arXiv:astro-ph/0701898v1 31 Jan 2007

Optical polarimetry of HH 135/HH 136[1]

C. V. Rodrigues[2], G. R. Hickel[3], A. H. Cerqueira[4], C. G. Targon[2]

ABSTRACT

We present optical linear polarimetry in the line of sight to HH 135/HH 136. The polarimetry of the field stars reveals two populations: one corresponds to a foreground interstellar component; the other originates in the interstellar medium in the vicinity of the Herbig-Haro pair and, therefore, can be used to study the magnetic field in the star forming region. Its direction is aligned with the jet of HH 135/HH 136, which could be an indication that the interstellar magnetic field is important in the outflow collimation. The interstellar magnetic field magnitude was estimated to be of order 90 μG. According to recent numerical simulations, an interstellar magnetic field of such strength can be important in the definition of the outflow direction. There is also evidence that the associated dark cloud has an elongation parallel to the magnetic field. Our image polarimetry of the extended emission associated with HH 135/HH 136 shows a centro-symmetric pattern pointing to the knot E of HH 136. Previous near infrared polarimetry traces a different illumination center, namely IRAS 11101−5829 - the probable exciting source of the system. This discrepancy can be explained if the YSO emission is completely blocked in optical wavelengths and the dominant optical source in the region is the knot E, whose nature is uncertain. A discussion of the spectral energy distributions of HH 136-E and IRAS 11101−5829 is presented.

Subject headings: ISM: Herbig-Haro objects — ISM: magnetic fields — techniques: polarimetric — ISM: individual (HH 135,HH 136)

---

[2] Instituto Nacional de Pesquisas Espaciais/MCT – Av. dos Astronautas, 1758 – 12227-010 - São José dos Campos - SP – Brazil – E-mail: claudiavr@das.inpe.br

[3] IP&D - Universidade do Vale do Paraíba – Av. Shishima Hifumi, 2911 – 12244-000 - São José dos Campos - SP – Brazil

[4] LATO-DCET/Universidade Estadual de Santa Cruz – Rodovia Ilhéus-Itabuna, km 16 – 45662-000 - Ilhéus - BA – Brazil

[1] Based on observations made at the Observatório do Pico dos Dias, Brazil, operated by the Laboratório Nacional de Astrofísica.

1. Introduction

Magnetic fields are believed to play a crucial role in the physics of jets and outflows in young stellar objects (YSOs). The models presently proposed to explain the outflow engine in low mass YSOs rely on a magneto-centrifugally driven mechanism (Shang et al. 2006 and references therein; Ferreira et al. 2006). Whether the magnetic field also defines the launching mechanism and properties of jets in high mass YSOs is still unclear. Some observational findings suggest that the formation of intermediate- to high-mass stars also proceeds via disk accretion as in its low-mass counterparts, powering similarly highly collimated outflows (Martí et al. 1993; Brooks et al. 2003; Davis et al. 2004; Gredel 2006). On the other hand, the interstellar (IS) magnetic field can be relevant in the maintenance of jets, as is suggested by the simulations of De Colle & Raga (2005). From an observational perspective, Ménard & Duchêne (2004), based on a sample of classical T Tauri stars, suggested that the objects with bright and/or long jets might have their disk axes parallel to the interstellar magnetic field.

HH 135 and HH 136 are very luminous Herbig-Haro (HH) objects discovered by Ogura & Walsh (1992), who presented optical imaging and spectroscopy of the sources. They are located in Eastern Carina in the southwest portion of the dark cloud DCld 290.4+01.9 (Hartley et al. 1986) near the bright-rimmed HII region BBW 47 (Brand et al. 1986). The recently discovered infrared cluster #59 from Dutra et al. (2003) is also coincident with the HH pair. A more complete description of the optical objects in this region is presented by Ogura & Walsh (1992). The estimated distance to the optical/infrared objects in this region is in the 2.7 – 2.9 kpc range. DCld 290.4+01.9, which has a size of $28' \times 12'$, is included in the CO(J=1-0) catalogue of Otrupcek et al. (2000). This line has a well defined Gaussian shape with a FWHM of 1.0 km s^{-1} and V_{LSR} = -19.8km s^{-1}.

Infrared observation were recently used to detect and study the physical properties of the H_2 jet (Gredel 2006). His H_2 and [Fe II] continuum-subtracted narrow band images nicely trace the line emission morphology in the outflow. A CO molecular outflow is also present (Ogura et al. 1998). Chrysostomou et al. (2006) present imaging circular polarimetry of HH 135/HH 136 which suggests a helical magnetic field in the outflow.

The emission knots of HH 135 and HH 136 are distributed in a practically straight line (Ogura & Walsh 1992). This could be interpreted as an evidence for two jets with a common origin. However, both jets are dominated by blue-shifted components, which has led Ogura & Walsh (1992) to propose that each HH object had a different source. Subsequent infrared polarimetry of the extended emission associated with the HH objects has shown that they have a common illuminating source, namely IRAS 11101−5829 (Tamura et al. 1997). The apparent contradiction of these two observations can be avoided by the scenario proposed by Ogura et al. (1998). In this picture, the HH 136 jet is deflected by a molecular cloud, changing from a red-shifted jet near the IRAS source to a blue-shifted one in its extremity (see Figure 5 of Ogura et al. 1998).

IRAS 11101−5829 is a luminous ($10^4 L_\odot$) YSO (Ogura & Walsh 1992) associated with molecular masers of different species (Braz et al. 1989; Te Lintel Hekkert & Chapman 1996; Walsh et al. 1997). Tamura et al. (1997) suggested that it is a Herbig Ae/Be stars encircled by a dust disk. In particular, the presence of a 6.7GHz methanol maser points to a high-mass YSO (Walsh et al. 1997). The masers profiles have V_{LSR} in the range -24 to -21 km s^{-1}, indicating a kinematic distance of approximately 3 kpc. This velocity is similar to that of the DCld 290.4+01.9, which suggests that the IRAS source and the dark cloud are associated. Molecular emission in CO and CS are reported by Zinchenko et al. (1995), Bronfman et al. (1996), and Ogura et al. (1998). The millimetric continuum image of this source shows evidence of more than one emission core (Hill et al. 2005). These data also indicate a total cloud mass of 230 M$_\odot$, consistent with the mass estimated by Ogura et al. (1998) of 150 M$_\odot$ using CO observations.

In this work, we present a study of the magnetic field in the interstellar medium (ISM) around the pair HH 135/HH 136 using polarimetric optical data. Polarimetry of the optical nebula associated with the HH 135/HH 136 is also obtained. A brief discussion of the IRAS 11101−5829 and HH 136-6 sources is presented. In Section 2, we describe the polarimetric data and their reduction. The results and discussion are presented in Section 3. In the last section, we summarize our findings.

2. Observations and data reduction

The observations have been done in 2005 February 12 with the 0.60-m Boller & Chivens telescope at the Observatório do Pico dos Dias, Brazil, operated by the Laboratório Nacional de Astrofísica, Brazil, using a CCD camera modified by the polarimetric module described in Magalhães et al. (1996). The employed technique eliminates the sky polarization (Piirola 1973; Magalhães et al. 1996). The CCD array used was a SITe back-illuminated, 1024×1024 pixels. The above telescope and instrumentation gives a field-of-view of $10\overset{\prime}{.}5 \times 10\overset{\prime}{.}5$ (1 pixel = $0\overset{\prime\prime}{.}62$). The data have been taken with an R_C filter. Polarimetric standards stars (Serkowski et al. 1975; Bastien et al. 1988; Turnshek et al. 1990) have been observed in order to calibrate the system and estimate the instrumental polarization. The measured values of the unpolarized standard stars were consistent with zero within the errors. Measurements using a Glan filter were also performed to estimate the efficiency of the instrument. They indicate that no instrumental correction is needed.

The reduction has been done using using the IRAF[2] facility. The images have been corrected for bias and flat-field. Counts in the ordinary and extraordinary images of each object were used to calculate the polarization using the method described in Magalhães et al. (1984). We have utilized the IRAF package PCCDPACK (Pereyra 2000) in the polarimetric analysis. We obtained the polarimetry of around 1 600 objects in the field-of-view. The results are presented and discussed in the following section.

The ordinary and extraordinary images of the extended emission associated with HH 135/HH 136 did not overlap allowing image polarimetry to be performed. It has been done considering circular apertures of 2 pixels ($\approx 1\overset{''}{.}2$) radius centered in points distant from each other by 4 pixels ($\approx 2\overset{''}{.}5$) in each CCD direction. The results are presented in Section 3.

In addition, we have performed differential photometry using as calibrators USNO objects in the image: they are 490 in total. With this we could estimate R magnitudes for all objects in the field.

3. Results and discussion

3.1. Magnetic field geometry

The direction of the magnetic field component in the plane of the sky can be traced by the position angle of the optical polarization. It is valid if one assumes that the polarization originates from the dicroic absorption of the star light by non-spherical interstellar grains aligned by the superparamagnetic mechanism (Davis & Greenstein 1951; Purcell & Spitzer 1971; a recent review on grain alignment can been found in Lazarian 2003).

Figure 1 shows the number distribution of the position angle of polarization, θ, for objects with $P/\sigma_P > 5$, which corresponds to $\sigma_\theta < 5\overset{\circ}{.}7$. We have also discarded objects that have positions superposed to the outflow. Using these restrictions, we reduce our sample to 303 objects. The distribution is clearly bimodal with peaks at approximately 55° and 100°. Therefore, we performed a two-Gaussian fit which is also shown in Figure 1. The fitted parameters and errors for bins of 10° are shown in Table 1 (lines 1 and 3). The results are statistically the same for smaller or larger bin widths. An inspection of the data shows that these two populations have distinct spatial distributions and polarization magnitudes. This is illustrated in Figures 2 and 3 in which we have respectively plotted the results for objects with polarization modulus smaller and larger than 1.5% (an arbitrarily chosen number). The objects with small values of polarization tend to be distributed in regions where the extinction is less pronounced (Figure 2 - left). In the right panel of Figure 2, we show the histogram of the position angle of this sub-sample as well as a Gaussian curve with the same mean and dispersion of that of Figure 1 centered at 100°. The agreement indicates that the population responsible for this peak in Figure 1 is well represented by polarization magnitudes smaller than 1.5%. The large vectors tend to be located in a strip running from the southwest to the northeast of the image which roughly corresponds to the dark cloud (Figure 3 - left). Again, one of the Gaussian curves in Figure 1 fits well the distribution of position angles.

---

[2] IRAF is distributed by National Optical Astronomy Observatories, which is operated by the Association of Universities for Research in Astronomy, Inc., under contract with the National Science Foundation.

Our interpretation of the above results is that the population with smaller values of polarization corresponds to foreground objects in the line of sight to the HH pair, while the more polarized objects have their polarization produced by grains associated with DCld 290.4+01.9, hence tracing the magnetic field alignment in the star forming region itself. To test this hypothesis, we have used the compilation of Heiles (2000) to verify the polarization behavior in a larger field-of-view. We selected the objects within a 5°× 5° field centered at HH 135 and with $P/\sigma_P > 3$ (85 objects). The number distribution of the position angles and a Gaussian fit are shown in Figure 4. The Gaussian parameters are presented in Table 1 (fourth line). In spite of the larger dispersion, the mean position angle of Heiles' objects compares well with that of our suggested foreground component. The mean polarization magnitude of Heiles' objects is 1%, which is also consistent with our data. These results corroborate the supposition that the population having a mean angle around 100° corresponds to the large scale, and probably foreground, ISM.

Another way to constrain the origin of each population is to determine the behavior of the polarization with distance, which, however, cannot be properly estimated with our data. From a statistical point of view, a faint object is generally farther than a bright one. So, an alternative, despite limited, approach is to check the polarization dependence with magnitude. Figure 5 shows that the polarization tends to increase with magnitude. This corroborates our hypothesis that the larger polarization values are associated with objects at larger distances.

The above discussion gives us confidence that the small polarization component is associated with the foreground ISM in the direction of the HH pair. Consequently, we should subtract this component from the observations to obtain the IS polarization produced by aligned dust *in* the star forming region. To estimate a value to the foreground component we have averaged the polarization of the objects with the observed polarization smaller than 1.5%. This totalizes 212 objects with a mean polarization of 0.59 ± 0.36% @ 93.4° (the quoted error is the standard deviation of the distribution). This value was subtracted from our sample of 303 objects. (We would like to note that all the arithmetics has been done using the Stokes parameters Q and U). The number distribution of θ for objects with $P/\sigma_P > 3$ is plotted in Figure 6. The parameters of the Gaussian fit is shown in the second line of Table 1. This distribution, which should represent the magnetic field orientation in the HH 135/HH 136 region, is similar to the uncorrected, but not the same. The mean position angle is at $41\overset{\circ}{.}9 \pm 1\overset{\circ}{.}2$.

The direction of the interstellar magnetic field found above can be compared with the geometry of the young stellar object, in particular, with the outflow direction. The jet position angle (from North to East - equatorial coordinates) has been estimated using the line joining IRAS 11101−5829 and a given line emitting knot. They are: HH 135, HH 136/A-B-D-H. There are other knots, but whose emission occurs mainly in the continuum, so they could not trace the jet. The adopted position angle for HH 136 is the average of its four knots. The resulting position angles are: $40\overset{\circ}{.}0$ for HH 135; and $37\overset{\circ}{.}9 \pm 0\overset{\circ}{.}2$ for HH 136. Therefore, the component of the interstellar magnetic field in the plane of sky ($\approx 42^\circ$) and the YSO outflow are approximately parallel.

An interstellar magnetic field aligned with the jet is the best configuration for the propagation of the outflow in the ISM, as recently demonstrated by De Colle & Raga (2005). These authors conducted two-dimensional numerical simulations of clumps (which, in their models, represent time-dependent ejection from YSOs) propagating in a magnetized ISM. They found that jets moving parallel to the ambient magnetic field can propagate to much longer distances when compared with those that propagate perpendicular to the magnetic field. They claim that this could explain the correlation found by Ménard & Duchêne (2004) for classical T Tauri stars; namely, the bright and long jets tend to be parallel to the interstellar magnetic fields. The jet associated with HH 135/HH 136 has a projected size of approximately 0.5 pc and high luminosity, so in this object we could be seeing the effect of a parallel IS magnetic field keeping the jet. On the other hand, Chrysostomou et al. (2006) have found evidence of a helical magnetic field in the outflow of HH 135/HH 136 based on infrared circular polarization, which can concur to collimate the jet. The present evidences, however, cannot state unambiguously which magnetic configuration is predominantly acting as the main large-scale collimating mechanism in this high-mass YSO.

The emission lines of H_2 and [Fe II] in HH 135/HH 136 indicate a fast, dissociative J-type shock (Gredel 2006). It is evidenced by the different space distributions of these emissions. In a J-type shock, the transverse (relative to the propagation direction) magnetic field is small. So the magnetic field direction inferred from our large-scale measurements may be similar to that in the ISM in which the shock propagates. However, we should again recall a possible helicoidal field in the outflow (Chrysostomou et al. 2006), which would produce a C-type shock or a J-type shock with precursors. More observations in order to constrain the detailed shock physical conditions - as, for instance, the H_2 v=0 transitions - may be helpful in disantangling the magnetic field geometry in the outflow region.

We could also ask if the geometry of DCld 290.4+01.9 has some correlation with the magnetic field. Figure 7 shows a $0.^{\circ}5 \times 0.^{\circ}5$ DSS2 Red image centered at DCld 290.4+01.9. The lines represent the contour plot of the flux at 100 μm from IRAS. HH 135/HH 136 can be seen in the lower right quadrant, northeast of the HII region BBW 47. The denser portion of the cloud - as illustrated by the obscuration at optical wavelengths and dust emission at infrared - seems to be elongated in the northeast-southwest direction. If this is true, the interstellar magnetic field, the HH outflow, and the cloud elongation are all nearly parallel. This configuration is similar to what occurs in Lynds 1641 (Vrba et al. 1988).

3.2. Magnetic field strength

The strength of the magnetic field in the plane of the sky, B, can be estimate using

$$B = (4\pi\rho)^{1/2} \frac{v}{\Delta\theta_B} , \qquad (1)$$

where: ρ is the mass density of the ISM; v, the one-dimensional turbulent velocity; and $\Delta\theta_B$, the dispersion of the magnetic field direction. This expression was proposed by Chandrasekhar & Fermi (1953) and relies on the equipartition of turbulent kinetic and magnetic energies and isotropy of the motions in the medium. The overall ideia behind this formula is still accepted (Heitsch 2005), notwithstanding different effects could lead the above equation not to be the best estimate of the actual field: large fluctuations of the magnetic field amplitude; acting of the nonmagnetic forces on the gas; inhomogeneity of the interstellar material (Zweibel 1996). Recent numerical simulations of polarimetric maps of molecular clouds indicate that this formula overestimates the magnetic field by a factor 2 (Ostriker et al. 2001; Padoan et al. 2001; Heitsch et al. 2001; Heitsch 2005; Matsumoto et al. 2006).

The value of $\Delta\theta_B$ in the star formation region can be estimated by the standard deviation of the fitted Gaussian to the number distribution of the position angle of the intrinsic polarization (see second line of Table 1). This number is, however, an overestimate of the dispersion of the magnetic field direction since it includes the observational error associated with the θ measurement. Following the procedure suggested by Pereyra & Magalhães (2005), we obtain a $\Delta\theta_B$ value of $13.^{\circ}3$. The turbulent velocity was considered that of the dark cloud and measured by Otrupcek et al. (2000) as 1 km s^{-1}. A total mass density of 1.4×10^{-20} g cm^{-3} has been estimated from the number density of H_2 presented in Zinchenko et al. (1995), which was based on CS(J=2-1) measurements near the IRAS source. Considering a factor of 0.5 to equation (1) - as discussed above - we obtain an interstellar magnetic field strength of 90 μG. However, we would like to note that this value should be interpreted as the order of magnitude of the field. The reason is twofold. On one hand, the observational values used in the magnetic field calculation have their own uncertanties. On the other hand, the values of the mass density, magnetic field dispersion, and turbulent velocity can be tracing different portions of the ISM. Heitsch (2005) obtained that a single estimation of B with the above procedure can be in error by a factor of 7. In addition, we would like to note that the above estimate of B should be associated with the large scale ISM around HH 135/HH 136, not with the outflow region. This value is larger than that measured in the diffuse ISM of a few μG, but it is in the range obtained for star forming regions (see, e.g., Gonatas et al. 1990; Chrysostomou et al. 1994).

Recently, Matsumoto et al. (2006) have studied the alignment of outflows with magnetic fields in clouds cores through numerical simulations. They found that the outflow tends to be aligned with the large-scale (> 5000 AU) magnetic field if the magnetic field *in the core* is larger than 80 μG. Our above estimate of 90 μG may be interpreted as the strength in the dark cloud, i.e., the initial magnetic field before the collapse (the B_o of Matsumoto et al. 2006). So the enhanced magnetic field in the collapsing core that originated the YSO has probably exceeded the limiting value of 80 μG, making plausible that in this region the geometry of the magnetic field in the original cloud determined the direction of the YSO outflow.

3.3. Imaging linear polarimetry of HH 135/HH 136

Figure 8 shows the imaging linear polarimetry of the emission nebula associated with HH 135/HH 136. The background image is from our data: the object is seen twice because of the beam splitting produced by the calcite block. Only measurements with $P/\sigma_P > 10$ are plotted. The vectors sizes show that the polarization can be as high as 30%. The position angles define a clear centro-symmetric pattern, typical of scattering, whose center has been calculated and coincides with knot HH 136-E (following the denomination of Ogura & Walsh 1992). From North to South, this knot is the second bright source in our image. The centers calculated using the data over the HH 135 region or the HH 136 region are the same.

HH 136-E is the brightest point in the R band image, having a magnitude of 14.37 mag. The knot B, the second brightest, has a magnitude of 14.78 mag, which corresponds to a flux 30% smaller than knot E. In both estimates we have used an aperture radius of 3 pixels ($= 1\farcs8$).

Our imaging R-band polarimetry indicates HH136-E as the illuminator center of the scattering pattern, so it is unequivocally associated with the region. Previous K-band polarimetry of the same region (Tamura et al. 1997) shows also a centro-symmetric pattern, but whose center is coincident with IRAS 11101−5829. The dominant source in the infrared region is NIRS 17 (Tamura et al. 1997 - see also Figure 5 of Gredel 2006), which is coincident with knot J. They suggested that the IRAS source is obscured from our view by an optically thick disk, which is evidenced by the "polarization disk", but illuminates the associated nebula through the optically thinner pole.

The optical depth of a dusty medium grows from infrared to optical wavelengths. Therefore, in the R band, the disk around the IRAS source can be optically thick even at its pole, thus preventing any flux to escape. This could explain why IRAS 11101−5829 is not the source of the optical light being scattered in the nebula. However, it remains as an open question the nature of the knot E.

HH136-E is the brightest R-band source in the outflow region and is associated with the infrared source NIRS 9, whose infrared colors are consistent with a pre-main-sequence object (Tamura et al. 1997). It has a very strong optical and infrared continuum, being practically absent of [S II], H_2 and [Fe II] emission (Gredel 2006; Ogura & Walsh 1992). This makes a Herbig-Haro nature quite improbable. In spite of the suggestion from Schmidt plates that knot E has an important Hα emission, no slit spectroscopy at its exact position has been done. The spectral energy distribution (SED) of the knots HH 136-A, HH 136-B, HH 136-E, and HH 135 can be done using DENIS (The Denis Consortium 2005) and 2MASS (Cutri et al. 2003) data, and our photometry. None of these sources are detected in longer wavelengths. The SED of knot E has a rising slope from I to K band. A black body fit to this curve provides a bolometric luminosity of $\approx$4 $L_\odot$, which would correspond to a ZAMS star of $\approx$2 $M_\odot$.

To explain the non-trivial radial velocity structure of the emission knots, and considering a same exciting source for HH 135 and HH 136 as indicated by previous K-band polarimetry, Ogura et al. (1998) have proposed a scenario in which one of the jets coming out from the exciting source is deflected by a nearby molecular cloud. The region of zero velocity is located around knots D, E, F, and G (Figure 9; see also Figure 7 of Ogura & Walsh 1992). In this region there is also a slightly increase of the ^{12}CO antenna temperature (Ogura et al. 1998). Besides, there is a MSX source between knot F and G, which could represent the point of collision. So another possibility to the nature of knot E would be the point where the jet collides with the molecular cloud.

A spectroscopic analysis of knot E as well as a detailed velocity study of the whole complex can probably shed some light in what is going on in this region and the true nature of this object.

3.4. Spectral energy distribution of IRAS 11101-5829

Figure 10 shows the SED of IRAS 11101-5829 based on literature data (see figure legend for the references). To estimate the bolometric luminosity of IRAS 11101−5829 we integrate a cubic spline to its SED which provides a value of 1.32×10^4 $L_\odot$ at a distance of 2.7 kpc. This is in agreement with previous estimates from Ogura & Walsh (1992) of 1.39×10^4 $L_\odot$ and from Walsh et al. (1997) of 1.59×10^4 $L_\odot$. Both of them are based on IRAS data, but consider different corrections. The above luminosity can be used to constrain the stellar mass. Using the massive stars evolutionary tracks of Bernasconi & Maeder (1996) for Z = 0.02, we estimate an interval of 11 – 25 $M_\odot$ for the mass of the central object. The higher masses are obtained if the object is very young, with a convective envelope.

The SED of an embedded source contains more information than just the luminosity of the central object. It results from the reprocessing of the stellar flux in the circumstellar environment. To exploit this aspect, we have used the recently available grid of models of Robitaille et al. (2006) to reproduce the observed SED of IRAS 11101−5829. We have concentrated on models whose parameters are:

- 1.0×10^4 $L_\odot$ < L < 1.4×10^4 $L_\odot$ - see discussion above;
- 11 $M_\odot$ < M < 25 $M_\odot$ - see discussion above;
- $i = 81.^\circ4$. Following Ogura et al. (1998), we consider that the jets make an angle with the plane of sky of $\approx 5^\circ$ and that the disk is perpendicular to the jets. Among the inclinations provided by Robitaille et al. (2006), we chose this value as a good approximation to IRAS 11101−5829;
- aperture = 100.000 AU. At a distance of 2.7 kpc, this corresponds to 37″. This is the largest aperture provided by the models. We have used it in order to approximate the the angular resolution of IRAS of ≈ 90″.

We have then 307 models which have been visually inspected. In doing this, we have selected the best 41 models for which we have calculated the χ^2 values. We have found that the models #3020025 and #3007152 produced the smallest χ^2. Table 2 shows the parameters of the models - we ask the reader to see a complete description of them in Robitaille et al. (2006). This simple modelling provides a object with a mass of ≈ 13 $M_{\odot}$, which puts the YSO near the ZAMS, with a age of 10^6 years.

The above result is unexpected considering the presence of jets that are typical of a younger object. To discuss that issue, we would like to initially recall the optical knot J (=NIRS 17). It is located at $1\farcs8$ from the IRAS 11101−5829 center position. However the error ellipse of this source is 19 x 5″, so it includes the optical/infrared source (see Figure 9). In the IR and optical, the knot emission is dominated by a strong continuum and does not have [S II] emission lines (Ogura & Walsh 1992; Gredel 2006). So a Herbig-Haro nature appears to be ruled out. On the other hand, the SED presents two maxima: in $\approx 60\mu$m and $\approx 2\mu$m. The above modelling has implicitly assumed that its near IR portion is caused by the circumstellar disk emission in the observer direction and therefore it should have the same center position of the far infrared emission. This might not be the case for HH 135/HH 136. As proposed by Tamura et al. (1997), a possible geometry is one in which the near infrared YSO emission (produced in disk) is obscured from the observer direct view, but it can flow from the pole and illuminate the nebular material in the jet region. We propose that the near IR SED (the knot J) is the YSO reflected light in the pole cavity, as seen in HH 46 (Dopita 1978). In such a case, if the YSO emission was isotropic, the knot J should trace the YSO's SED. However, we should recall that the YSO emits anisotropically. Supposing the adopted inclination is correct, the knot J should receive the emission from a smaller inclination which has a larger near IR component. So the SED for an inclination of ≈81° as seen from a direct view, should have smaller fluxes at these wavelengths. This would result in models having properties of a more embedded, consequently younger, object. To do a proper modelling it would be necessary to know the 3D configuration of the knot J and the YSO.

4. Conclusions

We have presented optical linear polarimetry of HH 135/HH 136 and the nearby ISM. Our main results are listed below.

- The polarization of stars mapping the magnetic field in the star forming region is nearly parallel to the Herbig Haro outflow. We suggested that the elongation of DCld 290.4+01.9 is also parallel to the magnetic field.

- We estimated the interstellar magnetic field strength as of order 90 μG.

- The interstellar magnetic field direction and magnitude are adequate to play a role in determining the outflow direction and keeping the jet collimation. However, a collimation by a helicoidal magnetic field in the jet region is not discarded.
- The R-band nebula associated with the HH pair has a clear reflection pattern whose center is the knot HH136-E. It seems to be a star, but its nature could not be securely determined and deserves more observational effort.
- A simple modelling of the IRAS 11101−5829 SED indicates a mass of 13 $M_\odot$ and an age of 1 Myr, which is inconsistent with the presence of jets in the object. A less evolved stage might be found if the knot J is assumed to be produced by the reflection of YSO light in the surrounding material.

CVR would like to thank J. W. Vilas-Boas for fruitful discussions. We acknowledge the use of: the USNOFS Image and Catalogue Archive operated by the United States Naval Observatory, Flagstaff Station (http://www.nofs.navy.mil/data/fchpix/); the SIMBAD database, operated at CDS, Strasbourg, France; the VizieR catalogue access tool, CDS, Strasbourg, France; the NASA's Astrophysics Data System Service; and NASA's *SkyView* facility (http://skyview.gsfc.nasa.gov) located at NASA Goddard Space Flight Center. Use of the images in Figures 2, 3, and 7 is courtesy of the UK Schmidt Telescope (copyright in which is owned by the Particle Physics and Astronomy Research Council of the UK and the Anglo-Australian Telescope Board) and the Digitized Sky Survey created by the Space Telescope Science Institute, operated by AURA, Inc, for NASA, and is reproduced here with permission from the Royal Observatory Edinburgh. This work was partially supported by Fapesp (CVR: Proc. 2001/12589-1).

Facilities: LNA:BC0.6m ()

REFERENCES

Bastien, P., Drissen, L., Ménard, F., Moffat, A. F. J., Robert, C., & St-Louis, N. 1988, AJ, 95, 900

Beichman, C. A., Neugebauer, G., Habing, H. J., Clegg, P. E., & Chester, T. J. 1988, Infrared astronomical satellite (IRAS) catalogs and atlases. Volume 1: Explanatory supplement, 1,

Bernasconi, P. A., & Maeder, A. 1996, A&A, 307, 829

Brand, J., Blitz, L., & Wouterloot, J. G. A. 1986, A&AS, 65, 537

Braz, M. A., Gregorio-Hetem, J. C., Scalise, E., Jr., Monteiro Do Vale, & J. L., Gaylard, M. 1989, A&AS, 77, 465

Bronfman, L., Nyman, & L.-A., May, J. 1996, A&AS, 115, 81

Brooks, K. J., Garay, G., Mardones, D., & Bronfman, L. 2003, ApJ, 594, L131

Chandrasekhar, S. & Fermi, E. 1953, ApJ, 118, 113

Chrysostomou, A., Hough, J. H., Burton, M. G., & Tamura, M. 1994, MNRAS, 268, 325

Chrysostomou, A., Lucas, P. W., Hough, J.H. & Tamura, M. 2006, in Protostars and Planets 2005, Eds. B. Reipurth, D. Jewitt, & K. Keil (Tucson: University of Arizona Press), in press

Cutri, R. M., et al. 2003, The IRSA 2MASS All-Sky Point Source Catalog, NASA/IPAC Infrared Science Archive. http://irsa.ipac.caltech.edu/applications/Gator/,

Davis, C. J., Varricatt, W. P., Todd, S. P. & Ramsay Howat, S. K. 2004, A&A, 425, 981

Davis, L. & Greenstein, J. L. 1951, ApJ, 114, 206

De Colle, F. & Raga, A. C. 2005, MNRAS, 359, 164

Dopita, A. 1978, A&A, 63, 237

Dutra, C. M., Bica, E., Soares, J., & Barbuy, B. 2003, A&A, 400, 533

Egan, M. P., et al. 2003, VizieR Online Data Catalog, 5114, 0

Ferreira, J., Dougados, C., & Cabrit, S. 2006, A&A, 453, 785

Gonatas, D. P., Engargiola, G. A., Hildebrand, R. H., Platt, S. R., Wu, X. D., Davidson, J. A., Novak, G., Aitken, D. K. & Smith, C. 1990, ApJ, 357, 132

Gredel, R. 2006, A&A, 457,157

Hartley, M., Manchester, R. N., Smith, R. M., Tritton, S. B., & Goss, W. M. 1986, A&AS, 63, 27

Heiles, C. 2000, AJ, 119, 923

Heitsch, F. 2005, ASP Conf. Ser. 343: Astronomical Polarimetry: Current Status and Future Directions, 343, 166

Heitsch, F., Zweibel, E. G., Mac Low, M.-M., Li, P., & Norman, M. L. 2001, ApJ, 561, 800

Hill, T., Burton, M. G., Minier, V., Thompson, M. A., Walsh, A. J., Hunt-Cunningham, M., & Garay, G. 2005, MNRAS, 363, 405

Lazarian, A. 2003, Journal of Quantitative Spectroscopy and Radiative Transfer, 79, 881

Magalhães, A. M., Benedetti, E., & Roland, E., 1984, PASP, 96, 383

Magalhães, A. M., Rodrigues, C. V., Margoniner, V. E., Pereyra, A., & Heathcote, S., 1996, in ASP Conf. Ser. 97, Polarimetry of the Interstellar Medium, Eds. W. G. Roberge & D. C. B. Whittet (San Francisco:ASP), 118

Martí, J., Rodríguez, L. F., & Reipurth, B. 1993, ApJ, 416, 208

Matsumoto, T., Nakazato, T., & Tomisaka, K. 2006, ApJ, 637, L105

Ménard, F. & Duchêne, G. 2004, A&A, 425, 973

Ogura, K., Nakano, M., Sugitani, K., & Liljeström, T. 1998, A&A, 338, 576

Ogura, K. & Walsh, J. R. 1992, ApJ, 400, 248

Ostriker, E. C., Stone, J. M., & Gamie, C. F. 2001, ApJ, 546, 980

Otrupcek, R. E., Hartley, M., & Wang, J.-S. 2000, PASA, 17, 92

Padoan, P., Goodman, A., Draine, B. T., Juvela, M., Nordlund, Å, & Rögnvaldsson, Ö. E. 2001, ApJ, 559, 1005

Pereyra, A., 2000. Dust and Magnetic Fields in Dense Regions of the Interstellar Medium, PhD Thesis, Univ. São Paulo

Pereyra, A., & Magalhães, A. M. 2005, in AIP Conf. Proc. 784, Magnetic Fields in the Universe, ed. E. M. de Gouveia dal Pino, G. Lugones, & A. Lazarian (Melville: American Institute of Physics), 743

Piirola, V., 1973, A&A, 27, 383

Purcell, E. M., & Spitzer, L. J. 1971, ApJ, 167, 31

Robitaille, T. P., Whitney, B. A., Indebetouw, R., Wood, K., & Denzmore, P. 2006, ApJS, 167, 256

Serkowski, K., Mathewson, D. L., & Ford, V. L. 1975, ApJ, 196, 261

Shang, H., Li, Z.-Y., & Hirano, N. 2006, in Protostars and Planets 2005, Eds. B. Reipurth, D. Jewitt, & K. Keil (Tucson: University of Arizona Press), in press

Tamura, M., Hough, J.H., Chrysostomou, A., Itoh, Y., Murakawa, K., & Bailey, J. A. 1997, MNRAS, 287, 894

Te Lintel Hekkert, P., & Chapman, J. M. 1996, A&AS, 119, 459

The Denis Consortium 2005, VizieR Online Data Catalog, 1, 2002

Turnshek, D. A., Bohlin, R. C., Williamson, R. L. II, Lupie, O. L., Koornneef, J., & Morgan, D. H. 1990, AJ, 99, 1243

Vrba, F. J., Strom, S. E., & Strom, K. M. 1988, AJ, 96, 680

Walsh, A. J., Hyland, A. R., Robinson, G., & Burton, M. G. 1997, MNRAS, 291, 261

Zinchenko, I., Mattila, K., & Toriseva, M. 1995, A&AS, 111, 95

Zweibel, E. G. 1996, in ASP Conf. Ser. 97, Polarimetry of the Interstellar Medium, Eds. W. G. Roberge & D. C. B. Whittet (San Francisco:ASP), 486

This preprint was prepared with the AAS LATEX macros v5.2.

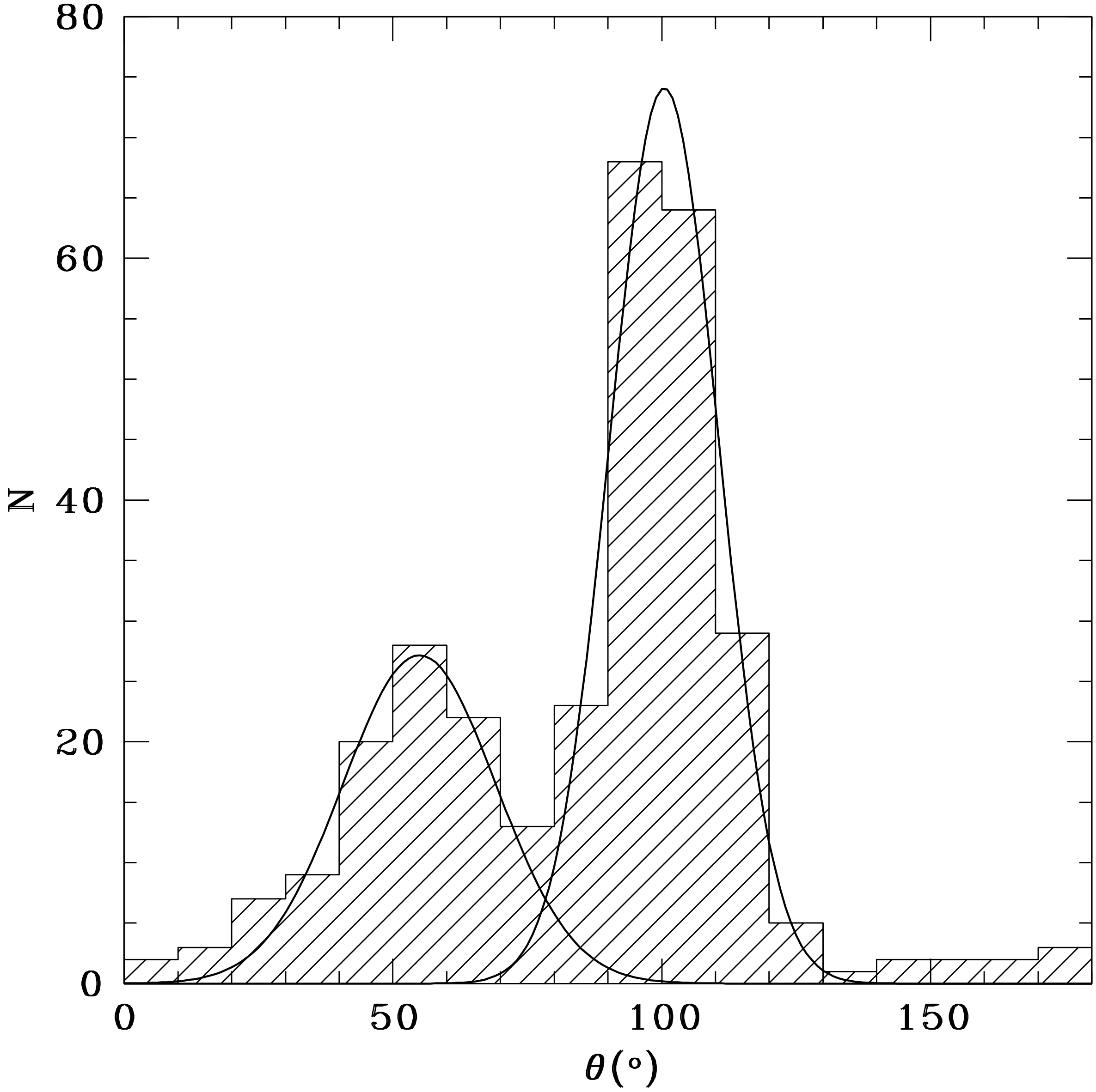

Fig. 1.— Histogram of the position angle of the observed polarization for fields stars with $P/\sigma_P > 5$ in the line-of-sight to HH 135/HH 136. A two-Gaussian fit is shown, whose parameters can be found in Table 1.

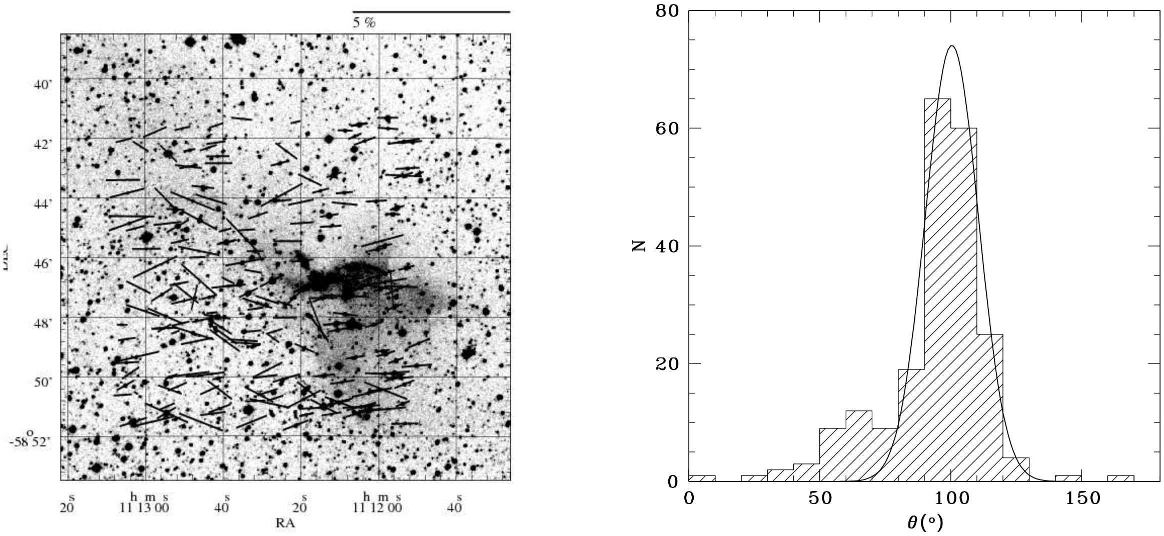

Fig. 2.— Polarimetry of field stars in the line of sight to HH 135/HH 136 with $P/\sigma_P > 5$ and $P < 1.5\%$. (Left) The vectors represent the direction and magnitude of the polarization whose scale is presented in the upper right of the figure. The background image is from the DSS2/Red. The epoch of the coordinates is 2000.0. (Right) Number distribution of the position angle of polarization for the same sample. The full line is one of the Gaussian curves obtained in the 2-Gaussian fit of Figure 1.

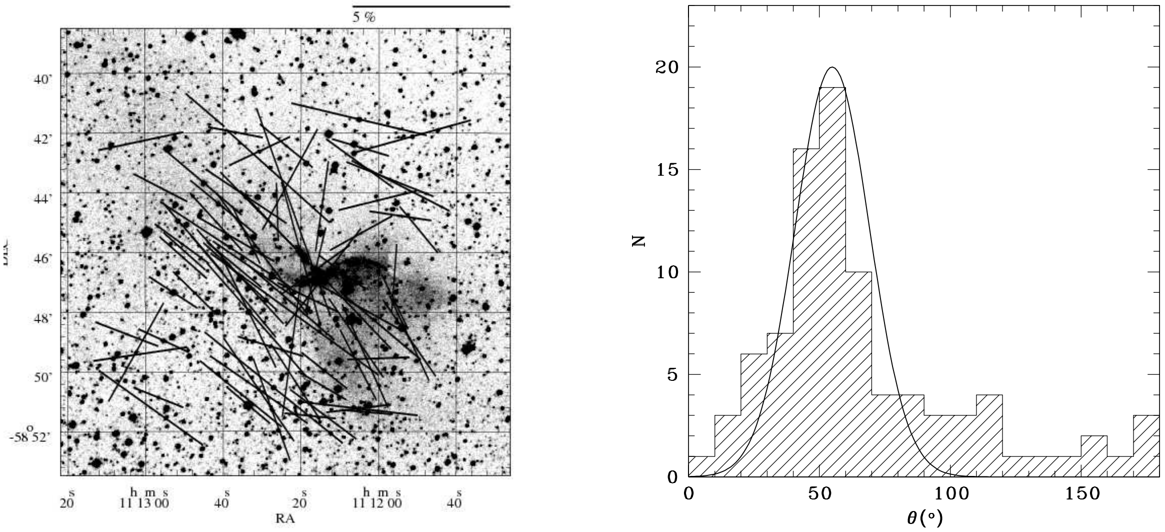

Fig. 3.— The same as Figure 2 for stars with $P/\sigma_P > 5$ and $P > 1.5\%$.

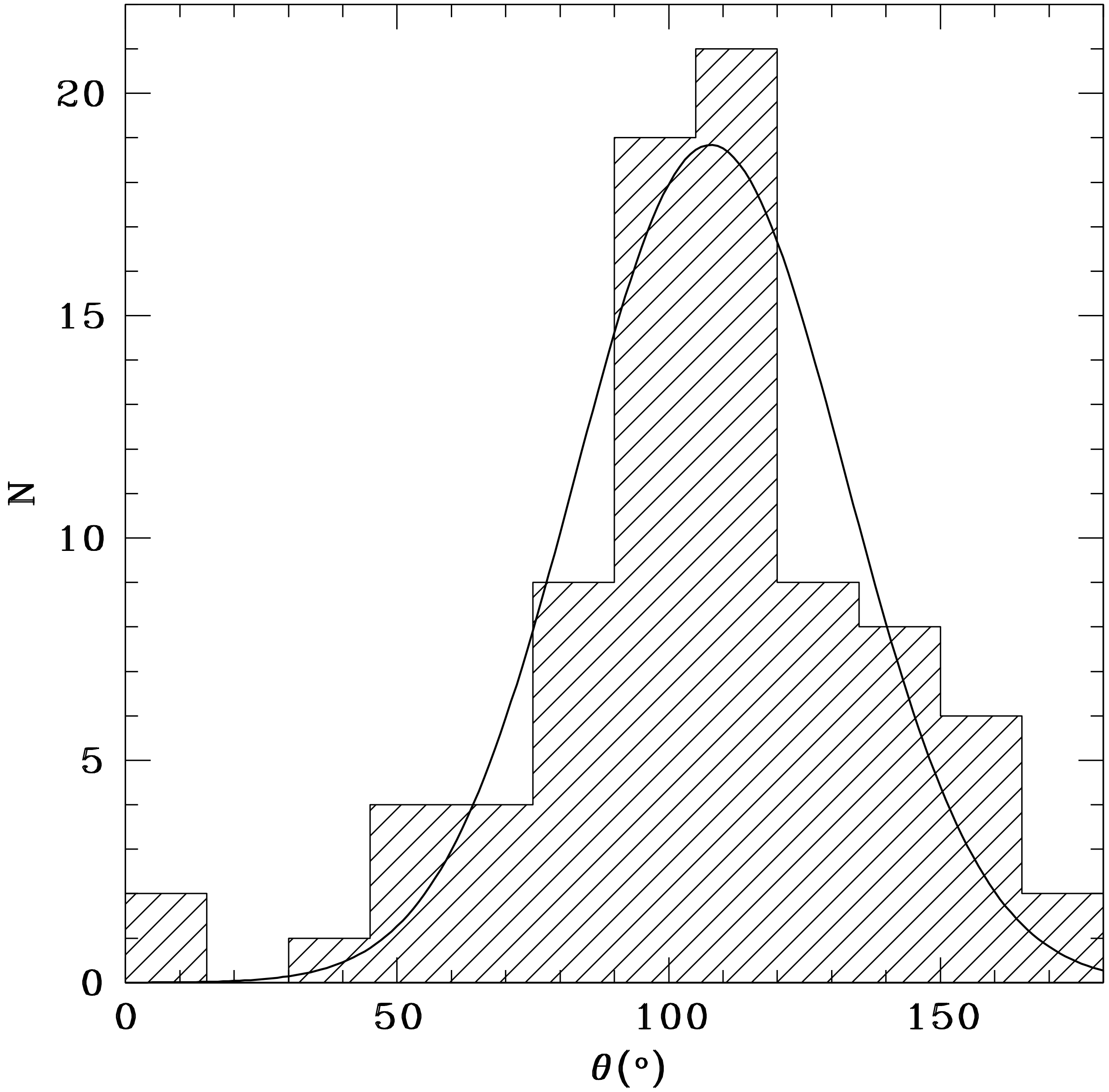

Fig. 4.— Number distribution of position angle of polarization for objects in the Heiles (2000)'s catalog within a 5°× 5° field-of-view centered at HH 135 and with $P/\sigma_P > 3$. A Gaussian fit is also shown - see Table 1 for the parameters.

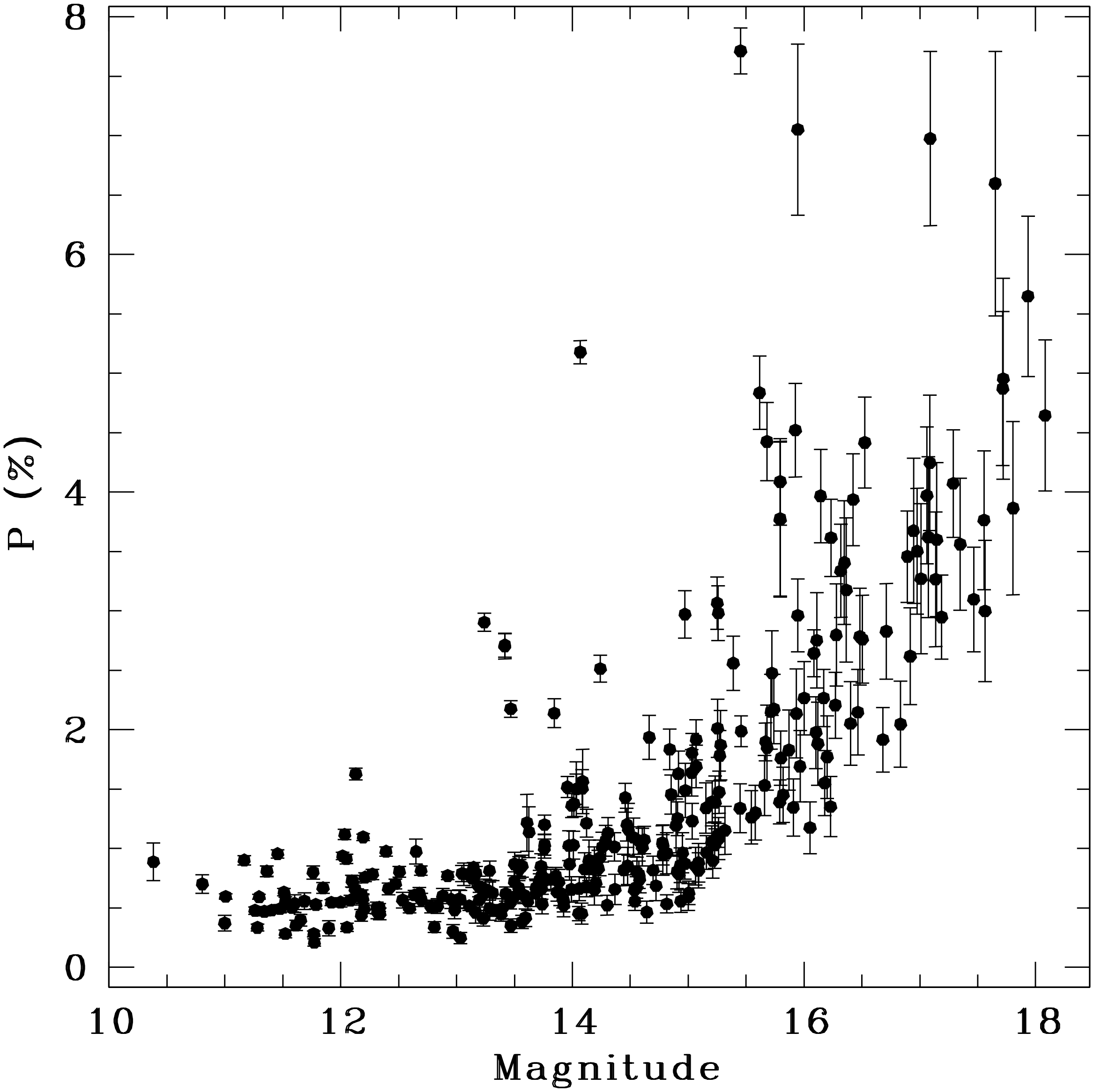

Fig. 5.— R-band polarization versus magnitude for objects with $P/\sigma_P > 5$.

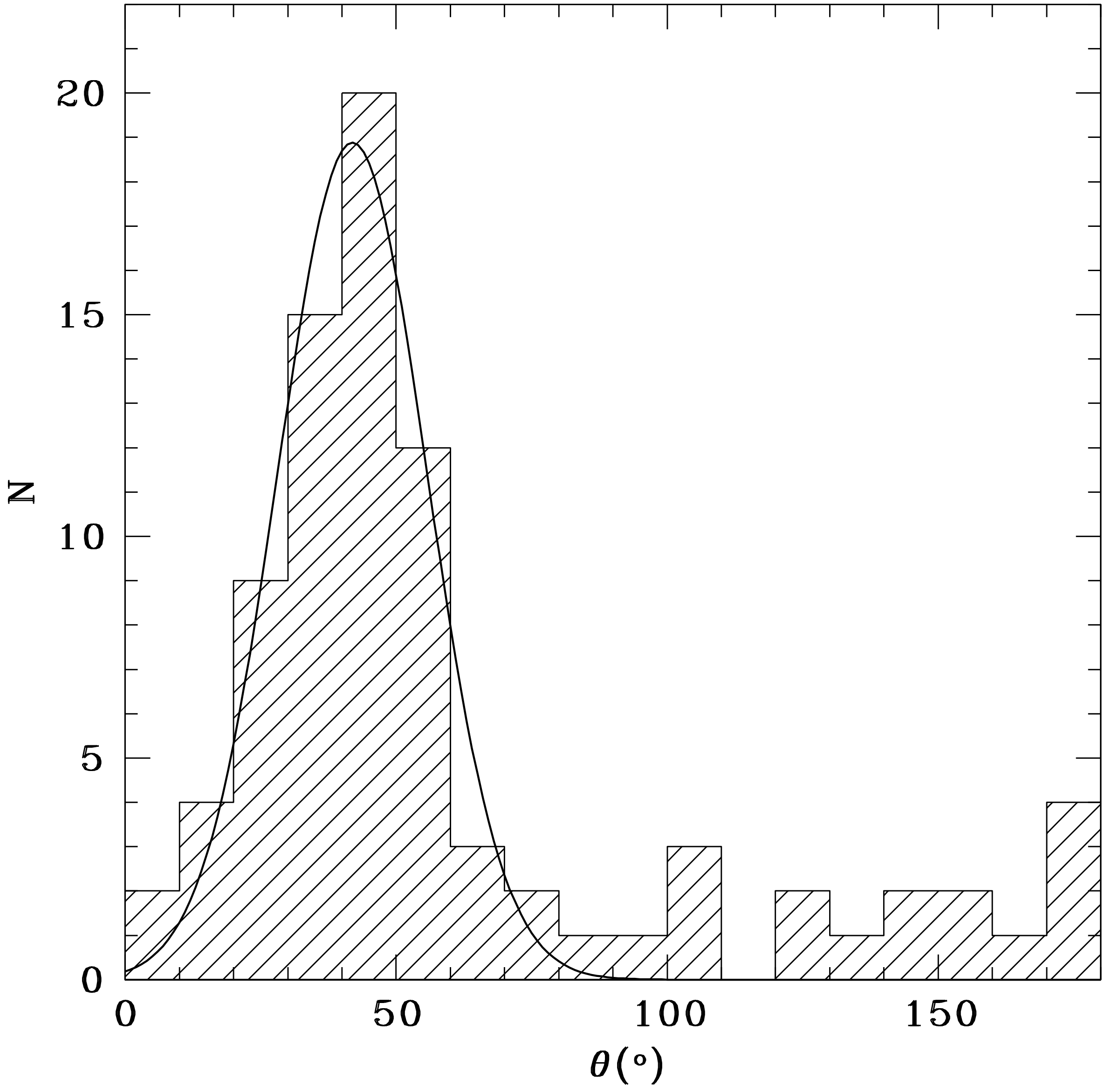

Fig. 6.— Number distribution of position angle of intrinsic polarization for objects in the line-of-sight to HH 135/HH 136 with $P/\sigma_P > 3$ after the foreground polarization subtraction. A Gaussian fit is also shown - see Table 1 for the parameters.

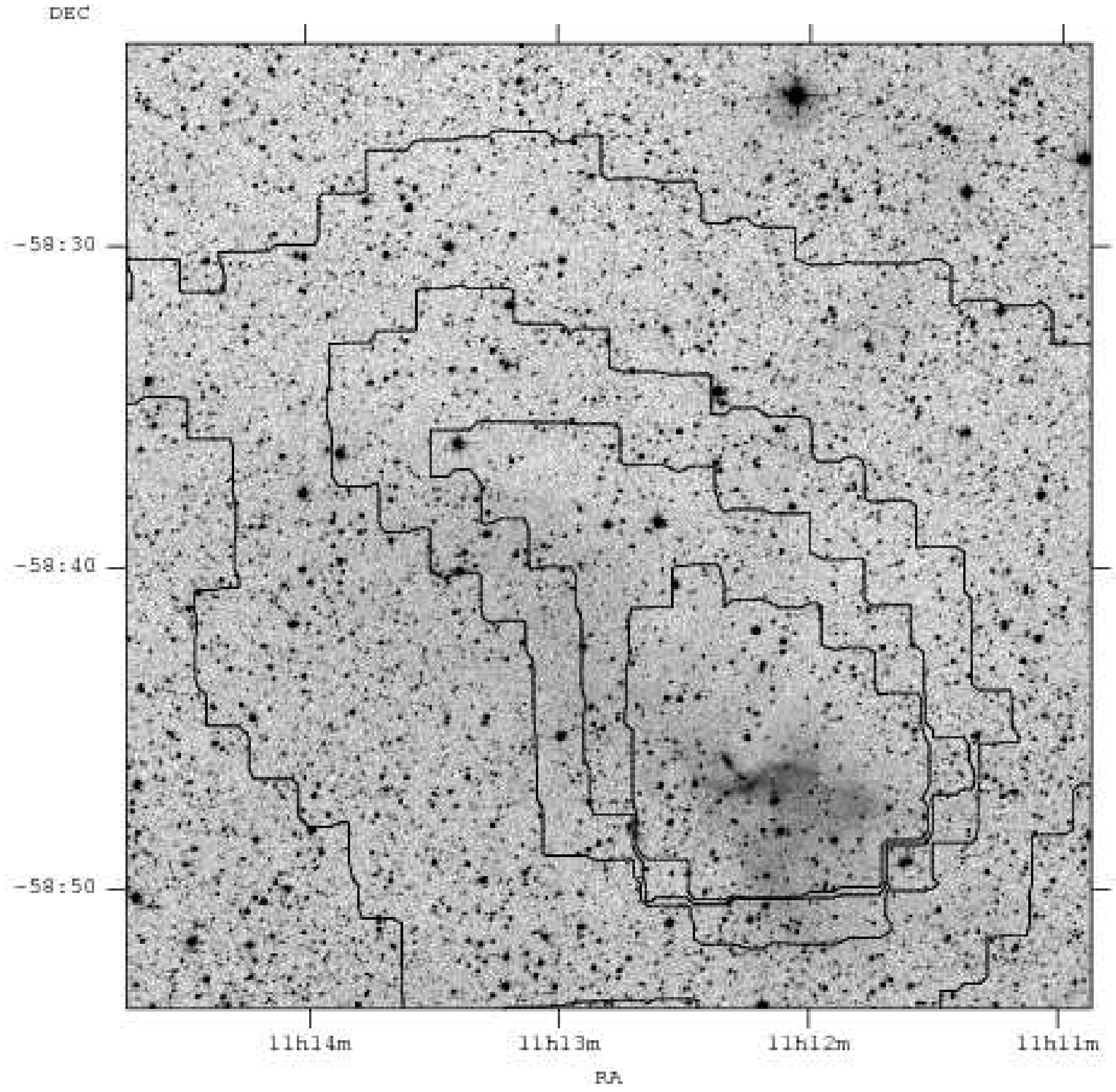

Fig. 7.— DSS2 Red view of a 0°.5 × 0°.5 region centered at DCld 290.4+01.9. The contour plot of 100 μm IRAS is seen superposed. The epoch of the coordinates is 2000.0.

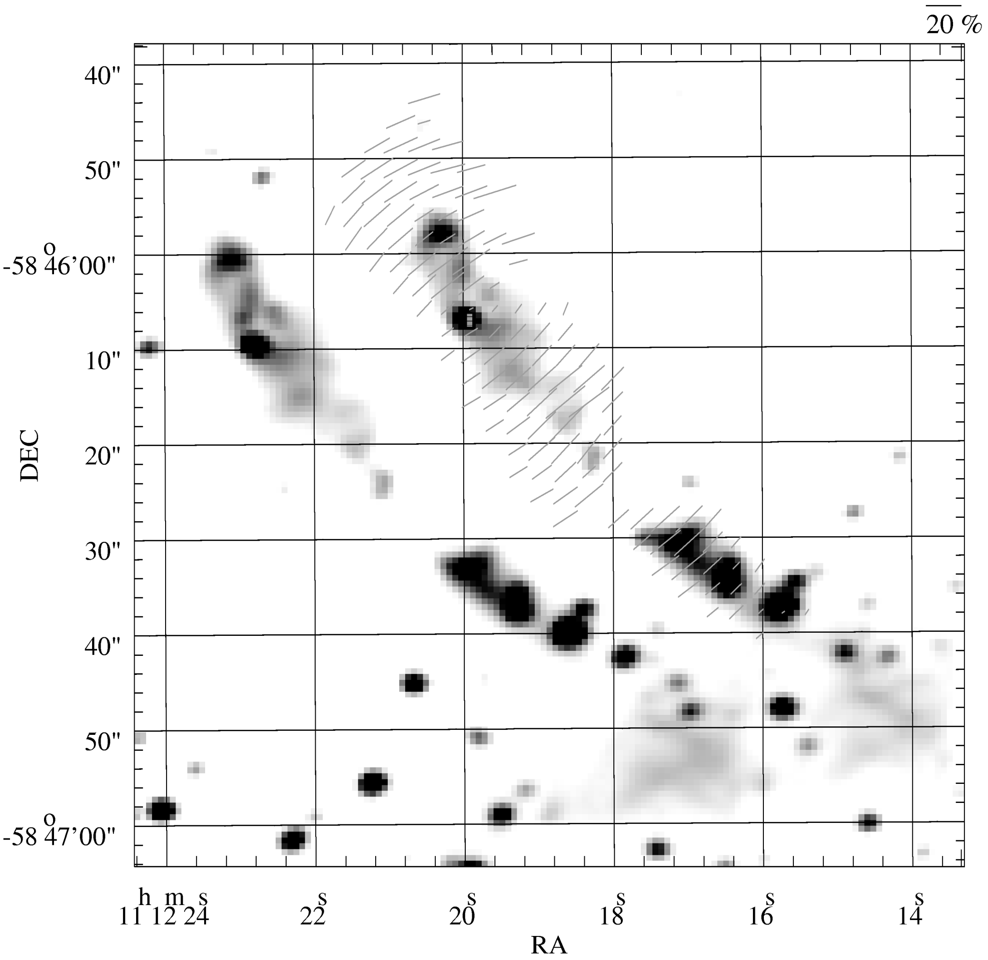

Fig. 8.— R-band imaging polarimetry of HH 135/HH 136. Only measurements with $P/\sigma_P > 10$ are shown. The polarization vectors, whose scale is presented in the top right corner, are superposed on our image. The two images correspond to the ordinary and extraordinary beams separated by the calcite block. The gray retangle marks the most likely position of the ilumination source. The coordinate scale is with respect to the right image and the vectors. The epoch is 2000.0.

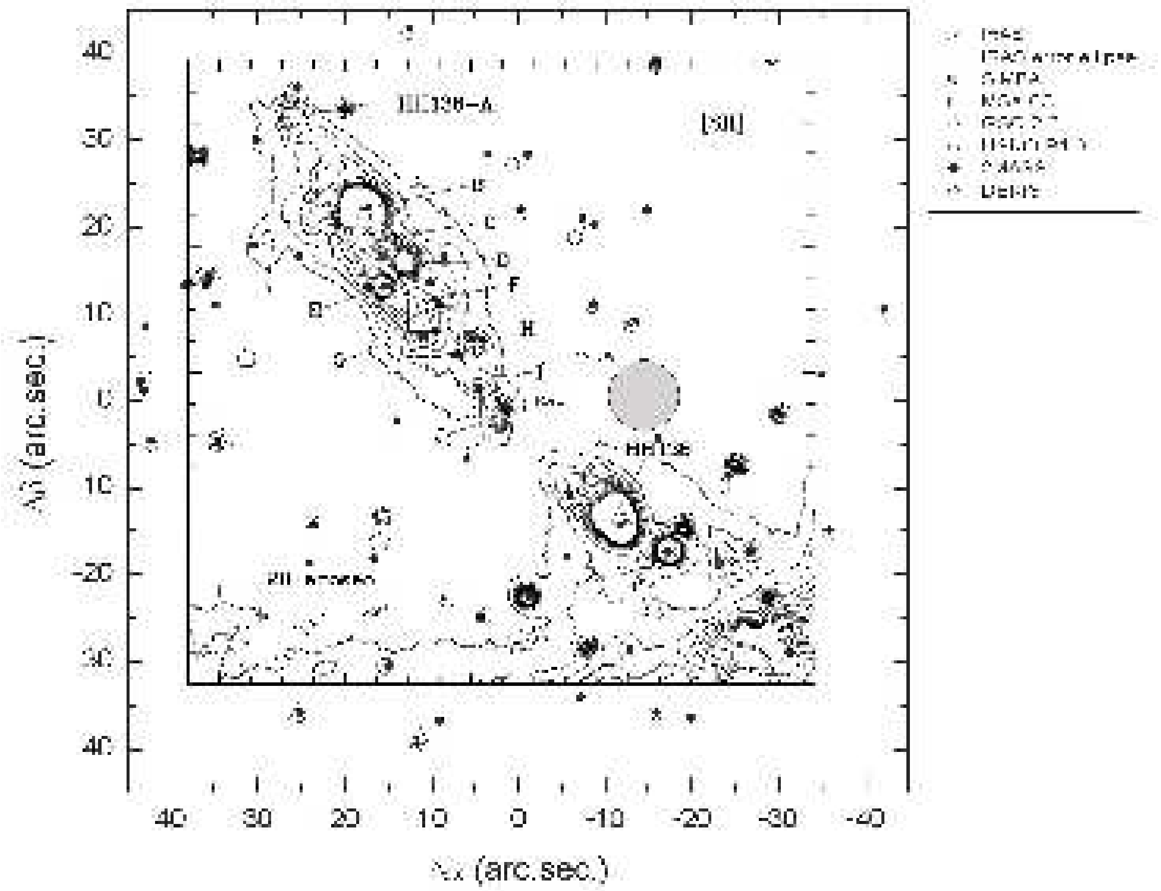

Fig. 9.— Different wavelengths sources in the region of HH 135/HH 136. The contour plot is the [SII] image (continuum included) from Gredel (2006). We use different symbols to represent the data origin: see legend at left.

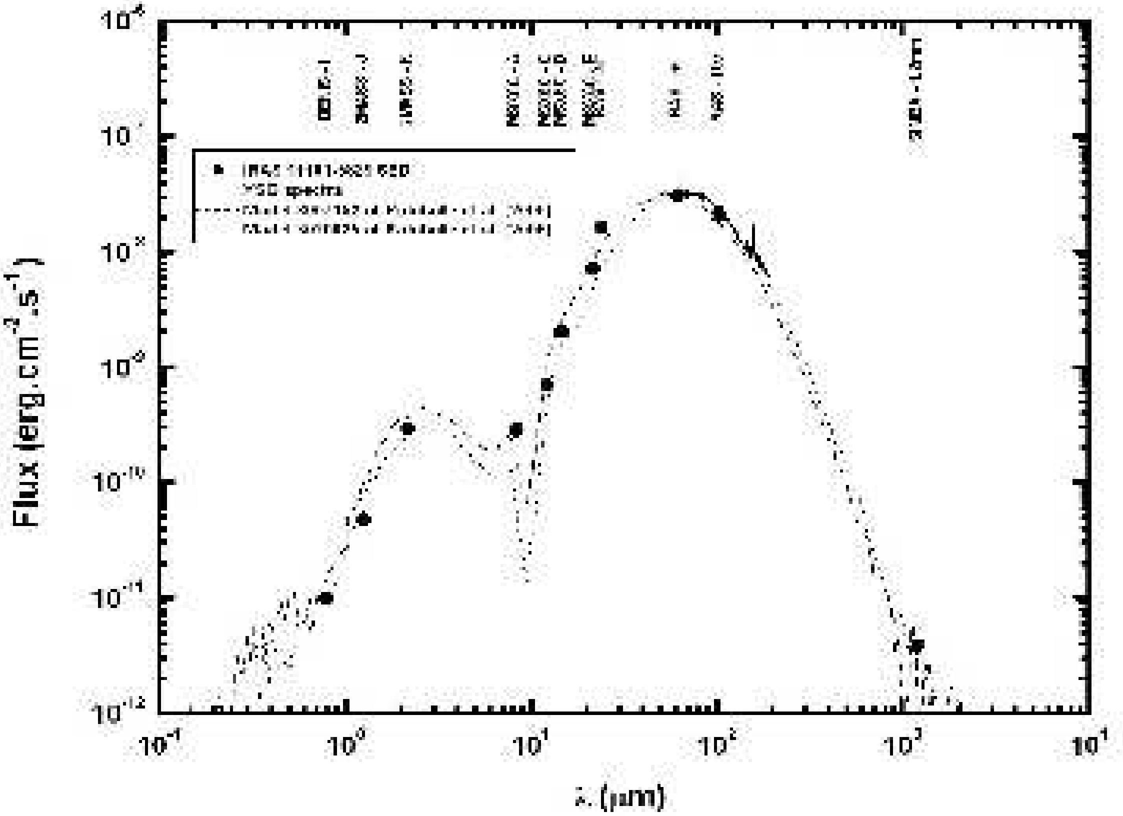

Fig. 10.— Spectral energy distribution of IRAS 11101-5829. The observational data are from the following resources. DENIS: The Denis Consortium (2005). 2MASS: Cutri et al. (2003). MSX: Egan et al. (2003). IRAS: Beichman et al. (1988). SIMBA: Hill et al. (2005). ISO spectrum from the ISO data archive (http://www.iso.vilspa.esa.es/ida/index.html). The dotted and traced lines represent two models from Robitaille et al. (2006) (see text for details).

Table 1: Parameters of the Gaussian fits to polarimetric data in the line-of-sight to HH 135/HH 136

Suggested origin	Mean (°)	Error (°)	Standard Deviation (°)	Error (°)	Data
HH 135/HH 136 region - with foreground	54.9	1.4	14.2	1.0	this work
HH 135/HH 136 region - foreground subtracted	41.9	1.2	13.8	1.0	this work
foreground ISM - 10′× 10′ field	100.5	0.4	10.2	0.3	this work
foreground ISM - 5°× 5° field	107.7	2.3	24.8	2.9	Heiles (2000)

Table 2: Parameters of Robitaille et al. (2006) models that best fit the IRAS 11101−5829 SED

Parameter Description	Value	
Model #	3007152	3020025
Stellar Mass ($\mathrm{M}_{\odot}$)	12.87	13.01
Stellar Radius ($\mathrm{R}_{\odot}$)	4.47	4.49
Stellar Temperature (K)	29,390	29,545
Envelope Accretion Rate ($\mathrm{M}_{\odot}$/yr)	1.04×10^{-3}	6.71×10^{-4}
Envelope Outer Radius (AU)	1.00×10^{5}	1.00×10^{5}
Cavity Angle (degrees)	31.8	29.4
Disk Mass ($\mathrm{M}_{\odot}$)	3.64×10^{-2}	1.69×10^{-2}
Disk Outer Radius (AU)	86.6	159
Disk Inner Radius (Rsub)	1.00	1.00
Disk Inner Radius (AU)	9.51	9.53
Scaleheight factor	0.837	0.996
Disk Flaring Power	1.073	1.104
Cavity density (cgs)	1.25×10^{-20}	1.12×10^{-20}
Ambient density (cgs)	6.09×10^{-21}	6.54×10^{-21}
Disk accretion rate ($\mathrm{M}_{\odot}$/yr)	5.72×10^{-6}	7.04×10^{-7}
Total A(V) along line-of-sight	4.90×10^{3}	0.99×10^{3}
Total Luminosity ($\mathrm{L}_{\odot}$)	1.38×10^{4}	1.38×10^{4}
Disk Scaleheight at 100AU	6.84	8.77